Diffeomorphic Susceptibility Artefact Correction of Diffusion-Weighted Magnetic Resonance Images

L. Ruthotto[1,2,3], H. Kugel[4], J. Olesch[1,5,6], B. Fischer[1,5], J. Modersitzki[1], M. Burger[3] and C.H. Wolters[2]

[1]Institute of Mathematics and Image Computing, University of Lübeck, Germany
[2]Institute for Biomagnetism and Biosignalanalysis, University of Münster, Germany
[3]Institute for Computational and Applied Mathematics, University of Münster, Germany
[4]Department of Clinical Radiology, University of Münster, Germany
[5]Fraunhofer MEVIS, Project Group Image Registration, Lübeck, Germany
[6]Graduate School for Computing in Medicine and Life Sciences, University of Lübeck, Germany

Abstract.

Diffusion weighted magnetic resonance imaging is a key investigation technique in modern neuroscience. In clinical settings, diffusion weighted imaging (DWI) and its extension to diffusion tensor imaging (DTI) is usually performed applying the technique of echo-planar imaging (EPI). EPI is the commonly available ultrafast acquisition technique for single-shot acquisition with spatial encoding in a Cartesian system. A drawback of these sequences is their high sensitivity against small perturbations of the magnetic field, caused, e.g., by differences in magnetic susceptibility of soft tissue, bone, and air. The resulting magnetic field inhomogeneities thus cause geometrical distortions and intensity modulations in diffusion weighted images. This complicates the fusion with anatomical T1- or T2-weighted MR images obtained with conventional spin- or gradient echo images and negligible distortion. In order to limit the degradation of diffusion weighted MR data we present here a variational approach based on a reference scan pair with reversed polarity of the phase- and frequency encoding gradients and hence reversed distortion.

The key novelty is a tailored nonlinear regularization functional to obtain smooth and diffeomorphic transformations. We incorporate the physical distortion model into a variational image registration framework and derive an accurate and fast correction algorithm. We evaluate the applicability of our approach to distorted DTI brain scans of six healthy volunteers. For all datasets, the automatic correction algorithm considerably reduced the image degradation. We show that after correction, fusion with T1- or T2-weighted images can be obtained by a simple rigid registration. Furthermore, we demonstrate the improvement due to the novel regularization scheme. Most importantly, we show that it provides meaningful, i.e., diffeomorphic geometric transformations, independent of the actual choice of the regularization parameters.

1. Introduction and Background

Within the last years, diffusion weighted magnetic resonance imaging has become one of the most important imaging methods especially in neuroscience research, but also in clinical routine. It is used either to obtain data on isotropic mean diffusivity, when it is commonly referred to plainly as DWI (diffusion weighted imaging, usually acquired with diffusion weighting gradients in three orthogonal directions), or to obtain additional directional information, referred to as DTI (diffusion tensor imaging), when gradients in more than 6 directions are measured. DWI allows the visualization of the mobility of water molecules within brain tissue (Stejskal & Tanner 1965, Basser et al. 1994), which is also clinically important, e.g., for early stroke detection (Warach et al. 1992) and characterization (Neumann-Haefelin et al. 1999) and for tumor characterization (Bergui et al. 2011, Hu et al. 2008). If with DTI directional information is also obtained, anisotropy measures of micro-structural integrity (Shimony et al. 1999, Wieshmann et al. 1999, Le Bihan et al. 2001, Deppe et al. 2007) and improved morphometric analysis of specific brain structures (Wiegell et al. 2003, Heidemann et al. 2010) is enabled. In addition, nerve fiber tracts and anatomical connectivity can be modeled (Conturo et al. 1999, Mori et al. 2000, Kaden et al. 2007, Makuuchi et al. 2009). Especially structural information obtained from DTI, e.g., fractional anisotropy, contributes to diagnosis of clinically relevant white matter alterations (Deppe et al. 2008, Wersching et al. 2010, Duning et al. 2011).

To speed up the acquisition of the relatively large number of images necessary to calculate a fractional anisotropy map or to visualize fiber bundle tracts, fast readout sequences are required. Moreover, to avoid motion and pulsation artifacts, diffusion weighted images are commonly acquired with a single-shot imaging method. The fast acquisition scheme of conventional echo planar imaging (EPI) is most frequently used for DWI and DTI. It is an ultra fast MRI sequence that allows acquisition times in the order of seconds for a whole brain volume (Stehling et al. 1991). This is achieved by sampling the entire space frequency domain of a selected slice with only one excitation using fast gradient blipping, which results in a very low acquisition bandwidth in the direction of the phase encoding gradient (Liang & Lauterbur 2000).

Owing to this low bandwidth, one limitation of EPI is the high sensitivity against small perturbations of the magnetic field (Chang & Fitzpatrick 1992, Jezzard & Clare 1999). These field inhomogeneities are inevitably caused by the fact that any object in an MR scanner distorts the field because its (magnetic) susceptibility is different from the surrounding medium (air in medical imaging). Furthermore, different tissues in the human body also have different susceptibilities (e.g., cerebrospinal fluid and bone) (Chang & Fitzpatrick 1992, Jezzard & Clare 1999, Morgan et al. 2004). The resulting field inhomogeneity scales with the B_0 field strength. The inhomogeneity affects the spatial encoding of the signal and degrades the reconstructed images by a geometrical deformation and a modulation of signal intensities (Chang & Fitzpatrick 1992). In EPI, the spatial displacement is dominant along the phase encoding direction and its extent

depends on acquisition bandwidth which can be controlled by measurement parameters, e.g, the readout time.

Image distortions severely complicate the fusion of information obtained by diffusion weighted images and anatomical information from T1- or T2-weighted images, obtained with conventional spin- or gradient echo sequences with negligible spatial distortion. This strongly influences the possibility to adequately model the human head in other neuroscience fields such as Electroencephalography (EEG) and Magnetoencephalography (MEG) source analysis (Wolters et al. 2006, Güllmar et al. 2010) and in simulation studies of brain stimulation techniques such as transcranial direct current stimulation (Holdefer et al. 2006) and transcranial magnetic stimulation (Opitz et al. 2011).

1.1. Existing approaches

Various approaches have been proven successful to limit the degradation of field distortions. The commonly used field map approaches include a direct measurement of the field-inhomogeneity by a reference scan and rectification of the distorted image data based on a physical distortion model, see (Jezzard & Balaban 1995, Andersson et al. 2001, Hutton et al. 2002) and (1). In addition to the problem of subject motion during the relatively long acquisition time, field map measurements demand regularization to overcome problems near tissue edges and regions with large inhomogeneities (Holland et al. 2010). Relatively noise-robust and accurate correction is achieved using the measurement of the point spread function (PSF) in MRI (Robson et al. 1997, Zeng & Constable 2002). However, measuring the PSF is very time consuming taking several minutes for a full brain volume (Holland et al. 2010), which motivated speed-ups using parallel imaging (Zaitsev et al. 2004) and simplified formulations such as Phase Labeling for Additional Coordinate Encoding (PLACE) (Qing-San Xiang 2007). Direct registration of EPI data to anatomical images have been proposed in (Merhof et al. 2007, Tao et al. 2009).

In this paper we follow a reversed gradient strategy for susceptibility correction that is based on inverted phase- and frequency-encoding gradients causing reversed distortion effects. This motivates the acquisition of two echo planar images that are identical apart from their opposite distortions (Chang & Fitzpatrick 1992, Morgan et al. 2004, Skare & Andersson 2005, Mohammadi et al. 2011). If the acquisition of the additional EPI can be restricted to a representation of basic geometry, e.g., by skipping measurements for redundant functional or diffusion information, the increase in scan time is kept to a minimum.

After image acquisition, the field-inhomogeneity is estimated such that the corrected datasets are as similar as possible. Different numerical schemes for this inverse problem have been proposed. Point-to-point references between the reference scans are established column-wise along the phase encoding direction (Chang & Fitzpatrick 1992, Morgan et al. 2004, Weiskopf et al. 2005). Image registration techniques, operating

in 3D, were successfully used to implement the reversed gradient scheme (Andersson et al. 2003, Skare & Andersson 2005). The field inhomogeneity was modeled with a set of basis functions thus yielding a finite dimensional optimization problem limiting the spatial variation of the field inhomogeneity estimate. By contrast, in a variational setting, optimization is carried out in function spaces and hence problems are infinitely dimensional. This allows highly nonlinear and very flexible transformation and omits, e.g., the specification of appropriate knot spacing in B-spline registration algorithms. The efficiency of variational algorithms for susceptibility correction is also supported by the recent works (Olesch et al. 2010, Holland et al. 2010), which will be our starting point.

1.2. Contribution and Outline

This paper summarizes and extends the variational approach (Holland et al. 2010) and our previous work of a diploma thesis (Ruthotto 2010) and a conference proceedings (Olesch et al. 2010) by a novel nonlinear regularization functional. This additional term directly controls the intensity modulation and ensured diffeomorphic geometrical transformations. Its formulation and discretization is motivated by (M.Burger et al. 2012), where we proposed a numerically sound scheme of a hyperelastic regularization energy for general image registration problems. In susceptibility correction of EPI, deformations are practically limited to the phase-encoding direction. We therefore derive a tailored and simplified version of the hyperelastic scheme. The new scheme still provides diffeomorphic transformations and thus meaningful intensity modulations and moderate computational costs.

Our novel algorithm is evaluated on a set of distorted DTI brain scans of six healthy volunteers obtained from widely applied clinical routine imaging protocol. The correction scheme is embedded into a DTI acquisition and processing pipeline to evaluate the impact on clinically relevant biomarkers. Our results indicate that, after susceptibility correction, registration to undistorted T1- or T2-weighted images can be performed by a simple rigid registration. In a numerical example on real data, we show that the novel regularization scheme can be crucial to guarantee meaningful solutions and is thus a valuable extension of (Olesch et al. 2010, Ruthotto 2010, Holland et al. 2010).

Our algorithm is embedded into the freely available image registration toolbox FAIR (Modersitzki 2009) and our Matlab code with example data is available at `http://www.siam.org/books/fa06`.

2. Materials and Method

2.1. Physical Distortion Model

In MRI the frequency of the resonance signal originating from each volume element depends on the exact magnetic field at that volume by the Larmor relationship. Spatial

encoding of the received signal is thus possible, if during acquisition of the resonance signal the magnetic field varies with position in a known way. During the slice-wise reconstruction of an image using a two-dimensional equidistant Fourier-transform method (Kumar et al. 1975, Edelstein et al. 1980) it is thus assumed that the switched magnetic field gradients, i.e., the frequency encoding gradient and the phase encoding gradient, are linear, and that the underlying static field is constant over the field of view, i.e., the resonance frequency depends linearly on position. Assuming a known field inhomogeneity $B : \Omega \to \mathbb{R}$, where $\Omega \subset \mathbb{R}^3$ is a domain, a forward model that relates the unobservable undistorted image $\mathcal{I} : \Omega \to \mathbb{R}$ to the observation $\mathcal{I}_1 : \Omega \to \mathbb{R}$ was introduced in (Chang & Fitzpatrick 1992). Let $\mathbf{v} \in \mathbb{R}^3$ denote the known direction of the spatial mismatch, the model reads

$$\mathcal{I}(\mathbf{x}) = \mathcal{I}_1(\mathbf{x} + B(\mathbf{x})\mathbf{v}) \cdot (1 + \partial_{\mathbf{v}} B) \quad \forall \mathbf{x} \in \Omega, \tag{1}$$

where $\partial_{\mathbf{v}}$ denotes the directional derivative of the scalar field B along $\mathbf{v}$. In addition to a geometrical displacement, the inhomogeneity also causes an intensity modulation represented by $(1 + \partial_{\mathbf{v}} B)$ (Chang & Fitzpatrick 1992).

The orientation and length of the vector $\mathbf{v}$ can be deducted and controlled by the measurement parameters of the imaging sequence (Chang & Fitzpatrick 1992). In EPI, severe artifacts are prominent and are most pronounced along the phase encoding direction, and negligible along the frequency encoding direction (Hutton et al. 2002). Hence, $\mathbf{v}$ points mainly along the phase encoding direction and its magnitude depends on the acquisition bandwidth. Most importantly in our application it is to note that the orientation of $\mathbf{v}$ is reversed when reversing the direction of the encoding switched field gradient (Chang & Fitzpatrick 1992).

One crucial assumption of correction techniques based on (1) is identified in (Chang & Fitzpatrick 1992). Namely, the measurement parameters have to be chosen such that the intensity modulation $1 + \partial_{\mathbf{v}} B$ remains positive. As this factor is the Jacobian determinant of the geometrical transformation $\mathbf{x} + B(\mathbf{x})\mathbf{v}$, this requirement corresponds to the invertibility of the mapping.

2.2. Variational approach to inhomogeneity correction

Given two echo planar images $\mathcal{I}_1$ and $\mathcal{I}_2$ measured with reversed spatial encoding gradients, the goal is to efficiently obtain the undistorted image $\mathcal{I}$ using (1) in an automatic post processing step. To this end, the unknown field inhomogeneity B is estimated such that $\mathcal{I}_1$ and $\mathcal{I}_2$ become as similar as possible to one another. Note, that ideally, because of the opposite distortion directions in $\mathcal{I}_1$ and $\mathcal{I}_2$, the inhomogeneity B satisfies

$$\mathcal{I}(\mathbf{x}) = \mathcal{I}_1(\mathbf{x} + B(\mathbf{x})\mathbf{v}) \cdot (1 + \partial_{\mathbf{v}} B) = \mathcal{I}_2(\mathbf{x} - B(\mathbf{x})\mathbf{v}) \cdot (1 - \partial_{\mathbf{v}} B) \quad \forall \mathbf{x} \in \Omega. \tag{2}$$

Hence, we introduce the distance functional

$$\mathcal{D}(B) = \frac{1}{2} \int_{\Omega} \left(\mathcal{I}_1(\mathbf{x} + B(\mathbf{x})\mathbf{v}) \cdot (1 + \partial_{\mathbf{v}} B) - \mathcal{I}_2(x - B(\mathbf{x})\mathbf{v})(1 - \partial_{\mathbf{v}} B) \right)^2 d\mathbf{x}. \tag{3}$$

Minimization of the distance functional with respect to $B : \Omega \to \mathbb{R}$ will in general not provide smooth estimates and fast convergence. We therefore regularize the problem by introducing prior knowledge on the smoothness of B. From the corresponding forward problem (De Munck et al. 1996) it can be seen that the inhomogeneity should be differentiable at least almost everywhere. Therefore, as in (Holland et al. 2010), we add a diffusion regularization to our problem

$$\mathcal{S}^{\text{diff}}(B) = \frac{1}{2}\int_{\Omega} |\nabla B(\mathbf{x})|^2 d\mathbf{x}. \tag{4}$$

This regularization functional can be shown to be sufficient with respect to the existence of a minimizer (Ruthotto 2010). However, this regularization does not ensure that the minimizer fulfills the assumption outlined in (Chang & Fitzpatrick 1992) and thus intensity modulations might be negative, see example in Sect. 3.3. Motivated by hyperelastic image registration schemes (Droske & Rumpf 2004, M.Burger et al. 2012) we aim to guarantee that the inhomogeneity estimate B satisfies

$$(1 + \partial_{\mathbf{v}} B(\mathbf{x})) \in]0, \infty[\text{ and } (1 - \partial_{\mathbf{v}} B(\mathbf{x})) \in]0, \infty[\text{ for almost every } \mathbf{x} \in \Omega, \tag{5}$$

which is equivalent to

$$\partial_{\mathbf{v}} B(\mathbf{x}) \in]-1, 1[\text{ for almost every } \mathbf{x} \in \Omega. \tag{6}$$

To this end, we introduce an additional nonlinear regularization term that directly controls the intensity modulations. The additional regularization functional $\mathcal{S}^{\text{jac}}$ reads

$$\mathcal{S}^{\text{jac}}(B) = \int_{\Omega} \phi(\partial_{\mathbf{v}} B(\mathbf{x}))\, d\mathbf{x}, \text{ with } \phi(z) = \frac{z^4}{1 - z^2}. \tag{7}$$

The function $\phi :]-1, 1[\to \mathbb{R}^+$ is symmetric, convex, grows rapidly as $|z| \to 1$, and has its minimum at $z = 0$, see Fig. 1. It is inspired by the control of volumetric changes in hyperelasticity, see (Droske & Rumpf 2004, M.Burger et al. 2012). We prove in the appendix that our model guarantees existence of diffeomorphic transformations.

To sum up, we obtain the inhomogeneity estimate B as the solution of the variational problem

$$\min_{B} \mathcal{J}(B) := \mathcal{D}(\mathcal{I}_1, \mathcal{I}_2; B) + \alpha \mathcal{S}^{\text{diff}}(B) + \beta \mathcal{S}^{\text{jac}}(B) \tag{8}$$

with regularization parameters $\alpha, \beta > 0$ that balance between distance reduction, smoothness of B and the range of the intensity modulations.

2.3. Discretization and Implementation

For the discretization of problem (8) we follow the guidelines from (Modersitzki 2009). For the intensity modulation and the additional regularization we re-use the concepts from the mass-preserving hyperelastic registration model in (Ruthotto 2010, Gigengack

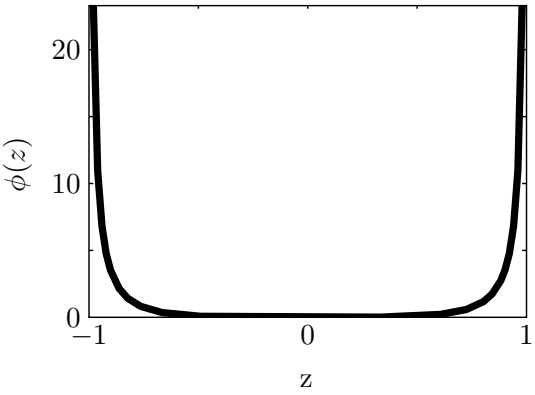

Figure 1. Plot of the proposed penalty function $\phi(z)$ acting on $\partial_{\mathbf{v}} B(\mathbf{x})$, see (7). The growth behavior of $\phi(z)$ to infinity as $|z| \to 1$ is crucial to ensure that the intensity modulations are positive almost everywhere and thus (5) is fulfilled. Since $1 \pm \partial_{\mathbf{v}} B(\mathbf{x})$ is the Jacobian determinant of the mapping $\mathbf{x} \pm B(\mathbf{x})\mathbf{v}$ this condition is equivalent to the diffeomorphy of the geometric transformation.

et al. 2012, M.Burger et al. 2012). Hence, the inhomogeneity is discretized on a nodal grid to allow direct access to the intensity modulation, which, as outlined, corresponds to the volumetric change induced by the transformation. As in (M.Burger et al. 2012) this relation is used and thus the Jacobian is computed based on this quantity. Compared to (M.Burger et al. 2012) considerable simplifications are realized, since the deformation in (8) is restricted to the direction $\mathbf{v}$. Consequently, the deformed voxels are trapezoids and computing volumes does not require a partition into 24 tetrahedra as in (M.Burger et al. 2012).

Our model is implemented as an extension to the freely available FAIR (Flexible Algorithms for Image Registration) toolbox in Matlab (Modersitzki 2009). The variational problem (8) is solved in a discretize-then-optimize approach on a hierarchy of levels representing coarse to fine discretizations of (8). The latter improves the stability against local minima and gives additional speed up as the prolongated solution from a coarse discretization serves as a good starting guess for the optimization problem on the next finer discretization.

The discretized problems are solved by Gauss Newton optimization (Nocedal & Wright 2000, Modersitzki 2009). Analytical first order derivatives are used and the Hessian is approximated such that its positive definiteness is assured. To determine the search direction, the approximated Hessian system is solved iteratively by a Preconditioned Conjugate Gradient (PCG) method. The step size is determined by a backtracked Armijo linesearch (Nocedal & Wright 2000) that guarantees sufficient descent, and updates satisfy (6). Standard criteria for automatic stopping of the optimization are employed, see (Modersitzki 2009), and the maximum number of iterations is set to 10 in our experiments.

For computationally expensive routines such as image interpolation and regularization we use parallelized C-Code in a matrix free fashion. That is, operators

such as the Hessian are not represented by sparse matrices but their acting on a vector is described in functions. See, e.g., (Modersitzki 2009) for more details on this general concept. Hence, memory consumption is kept to a minimum and the algorithm runs within fast runtimes on a standard computer.

2.4. Measures for the quantification of the registration quality

We quantify the quality of our new correction approach based on two image based and two transformation based measures.

The relative reduction of the distance between the digital images I_1 and I_2 is measured using a discretization D of the distance measure in (3) as the fraction $D(B)/D(\mathbf{0})$, where $\mathbf{0} \equiv 0$ denotes zero displacement. A value of zero thus represents identical images after registration.

An alternative image based distance measure is the Normalized Cross Correlation ($\mathcal{NCC}$) of I_1 and I_2, i.e.,

$$\mathcal{NCC}(\mathcal{I}_1, \mathcal{I}_2) := \sum_{i,j,k} \left(\frac{I_1^{i,j,k} - \mu(I_1)}{\sigma(I_1)} \cdot \frac{I_2^{i,j,k} - \mu(I_2)}{\sigma(I_2)} \right)^2, \tag{9}$$

where $\mu(I) := (1/N) \sum_{i,j,k} I^{i,j,k}$, $\sigma^2(I) := \mu((I - \mu(I))^2)$, and N is the number of voxels. Extreme values for the $\mathcal{NCC}$ are 1 and -1, where a value of 1 indicates maximally correlated images.

The range of B measures the maximal deformation. Motivated by the regularity criterion (6), we consider it as important to additionally measure the range of $\partial_{\mathbf{v}} B$, which needs to be strictly between -1 and 1 for a diffeomorphic solution.

2.5. DTI processing pipeline

In order to validate the impact of our method on the spatial correspondence between the distorted DTI data and undistorted anatomical images like T1- and T2-weighted MRI, we embedded our correction model into an existing DTI processing pipeline. Using state-of-the-art methods from the publicly available package FSL (Smith et al. 2004), the DTI data is corrected for eddy currents. For improved assessment of the geometrical correspondences a brain segmentation is performed jointly based on the rigidly co-registered T1w and T2w images. To this end, the brain is segmented individually in both images using the `bet` routine (Smith et al. 2004). Subsequently, a joint segmentation into cerebrospinal fluid, white matter and gray matter is performed using the `fast` routine (Smith et al. 2004). Finally, the anatomical images and their segmentation are registered to the $b = 0$ weighted diffusion image using a rigid registration.

The inhomogeneity estimate is obtained once as the solution of (8) with $\mathcal{I}_1$ and $\mathcal{I}_2$ being the images acquired with "flat" diffusion gradient (diffusion weighting factor b = 0), but reversed spatial encoding gradients. Based on this estimate the remaining image volumes of the DTI data are corrected for inhomogeneity artifacts using `dtifit`

(1). Finally, diffusion tensors are reconstructed using (Smith et al. 2004). Comparison of the fractional anisotropy maps before and after correction serves as a measure for the overall quality of the correction, see Section 3.2.

2.6. Data acquisition

Whole-head structural and diffusion weighted MR images of six healthy subjects were measured on a 3T scanner (Gyroscan Intera/Achieva 3.0T, System Release 2.5 (Philips, Best, NL)). T1 weighted anatomical images were acquired with a 3D fast gradient echo sequence ('Turbo Field Echo'), with water-selective excitation (i.e., no fat signal), TR = 9.5 ms, TE 4.6 ms, FA = 9°, two signal averages, inversion prepulse every 1024 ms, acquired over a field of view (FOV) of 300 (FH) x 240 (AP) x 234 (RL) mm, in a matrix of 256×204×200, resulting in cubic voxels of 1.17 mm edge length. T2w images with the same resolution were acquired with a multislice Turbo Spin-Echo sequence, TR = 5465 ms, TE = 60 ms, FA = 90°, 1 signal average, echo train length 6, 180 sagittal slices, 1.17 mm thick without slice gap, FOV 300 (FH) x 240 (AP) mm, matrix 256×240.

Diffusion weighted MRI was performed using a Steijskal-Tanner spin-echo EPI sequence. Geometry parameters were: FOV 240 x 240 mm for 36 transverse slices, 3.6 mm thick, with a square matrix of 128, resulting in voxels of 1.875 x 1.875 x 3.6 mm, interpolated by zero filling to 0.9375 x 0.9375 x 3.6 mm. Contrast parameters were TR = 9473 ms, TE = 95 ms. One volume was acquired with diffusion sensitivity $b = 0$ s/mm^2, and 20 volumes with $b = 1000$ s/mm^2 using diffusion weighted gradients in 20 directions, equally distributed on a sphere according to the scheme of Jones (Skare et al. 2000, Jones 2004). Bandwidth in phase encoding direction - selected as anterior posterior - was 9.1 Hz/pixel, in frequency encoding direction it was 1675 Hz/pixel.

With one exception (difference 14%), the difference of mass (i.e., the integral of the intensities over the image domain between $\mathcal{I}_1$ and $\mathcal{I}_2$) was less than 1.5%. Although only the image pair with "flat" diffusion gradient, i.e., $b = 0$ s/mm^2, is required for our correction, we acquired two full data sets with reversed phase- and frequency encoding gradients for each subject to investigate the impact of the correction on the localization of the fractional anisotropy, see Section 3.2 and Section 4.

2.7. Computational platform

All computations were run on a Linux PC with a six core Intel Xeon X5670 @2,93 GHz using Matlab 2010b.

3. Results

3.1. Susceptibility correction results

We first aim to correct the six diffusion tensor datasets by applying the novel algorithm on the baseline images without diffusion weighting. For all datasets, we use the same

regularization parameters ($\alpha = 20$ and $\beta = 10$), see Section 3.3 for the motivation of this choice. As the image resolution is very anisotropic we did not reduce the number of slices in the multi-level approach. Thus, four steps with discretizations on $m_1 = (32, 32, 36), m_2 = (64, 64, 36), m_3 = (128, 128, 36)$ and $m_4 = (256, 256, 36)$ are performed.

Detailed correction results are summarized in Table 1. Across all datasets, the distance between $\mathcal{I}_1$ and $\mathcal{I}_2$ with respect to $\mathcal{D}$ was reduced considerably (2nd column in Table 1). The similarity with respect to the $\mathcal{NCC}$ almost improved to the optimal value of 1 (3rd and 4th columns in Table 1). For all six datasets a smooth inhomogeneity estimate was found and, indicated by the range of the directional derivative $\partial_{\mathbf{v}} B$ being in $[-0.92, 0.91]$, the regularity criterion (6) was fulfilled for all subjects (5th column in Table 1).

The overall range of B was comparable for all datasets with a maximum of 30.6 mm in dataset DTI-5 (6th column in Table 1). Maximal runtime of the algorithm was 133 seconds on our test platform (7th column in Table 1).

In Figure 2 we visualize the correction results for dataset DTI-3. It can be seen that the estimated field inhomogeneity B considerably reduces the geometrical mismatch between $\mathcal{I}_1$ and $\mathcal{I}_2$. Note the strong reduction of the remaining intensities in the difference images ($|\mathcal{I}_1 - \mathcal{I}_2|$) after correction (right column of the right 3-columns-block in Figure 2) when compared to before correction (right column of the left 3-columns-block in Figure 2). The interpolation lines are smooth and do not overlap, which indicates that the mapping is diffeomorphic.

3.2. DTI Pipeline and Registration

We investigated the impact of our method on the spatial correspondence between the distorted DTI data and T1- and T2-weighted MRI. Figure 3 (a) shows both

Table 1. Results of susceptibility correction for the six DTI datasets: Reduction of the distance measure $\mathcal{D}$ (2nd column), Normalized Cross-Correlation between $\mathcal{I}_1$ and $\mathcal{I}_2$ before ($\mathcal{NCC}(0)$, 3rd column) and after ($\mathcal{NCC}(B)$, 4th column) registration. Range $\partial_{\mathbf{v}} B$ (5th column) as a measure of registration regularity and range of B (6th column) as a measure of the maximal deformation. Runtime (7th column) and number of iterations on the different levels (from coarse to fine) of the multi-level optimization approach (8th column).

Dataset	$\frac{\mathcal{D}(B)}{\mathcal{D}(0)}$	$\mathcal{NCC}(0)$	$\mathcal{NCC}(B)$	Range $\partial_{\mathbf{v}} B$	Range(B)	runtime[sec]	iterations
DTI-1	0.04	0.74	0.98	$[-0.92, 0.86]$	$[-18.5, 30.3]$	133	$[10, 4, 4, 6]$
DTI-2	0.04	0.74	0.98	$[-0.91, 0.89]$	$[-16.0, 28.8]$	100	$[10, 5, 3, 3]$
DTI-3	0.05	0.66	0.97	$[-0.89, 0.91]$	$[-24.1, 29.1]$	80	$[10, 6, 4, 2]$
DTI-4	0.05	0.69	0.97	$[-0.90, 0.84]$	$[-19.7, 24.1]$	70	$[10, 4, 3, 2]$
DTI-5	0.05	0.72	0.98	$[-0.91, 0.90]$	$[-14.1, 30.6]$	87	$[10, 3, 3, 3]$
DTI-6	0.04	0.72	0.98	$[-0.91, 0.89]$	$[-16.3, 22.8]$	63	$[10, 4, 3, 2]$

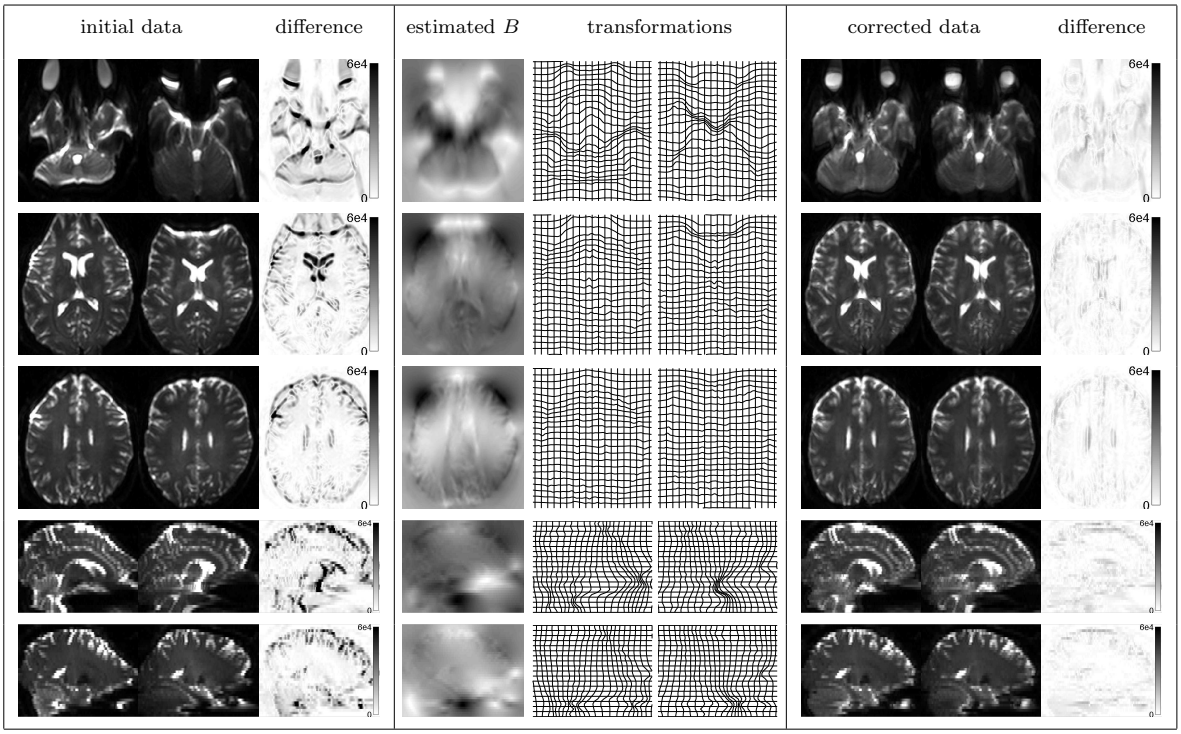

Figure 2. Distortion correction results for dataset DTI-3: Axial and saggital slices of the images $\mathcal{I}_1$ (left) and $\mathcal{I}_2$ (middle) and the difference image (right) before (left 3-columns-block) and after (right 3-columns-block) correction are visualized. The scale for the difference images was chosen identical before and after correction such that the reduction of the image distance is clearly visible. The middle 3-columns-block shows the estimated inhomogeneity B (left) and the two geometrical transformations represented by interpolation lines (middle and right).

$b = 0$ weighted diffusion images in an axial slice visualization, zoomed into the frontal brain region for better visibility for dataset DTI-3. Superimposed contour lines represent a white matter segmentation obtained from T1w and T2w-MRI are depicted in all subplots excluding (f) and (h). Geometrical mismatch of the uncorrected EPI measurements and T1w and T2w images is most pronounced in frontal regions and around the Corpus Callosum. After correction, the geometrical correspondence improves crucially, see visualizations in (c). Figure 3 (e) illustrates the fractional anisotropy (FA) maps derived from the DTI measurements with reversed spatial encoding gradients without susceptibility correction. The absolute difference visualization in (f) reveals the geometrical mismatch of the FA maps, which, as to be expected from (a), is severe in the region of the Corpus Callosum. After applying the proposed susceptibility correction pipeline the localization of the fractional anisotropy on the segmented white matter improves notably, see (g). This also manifests in a decay in the absolute difference image visualized with identical colormaps in (h) and (f).

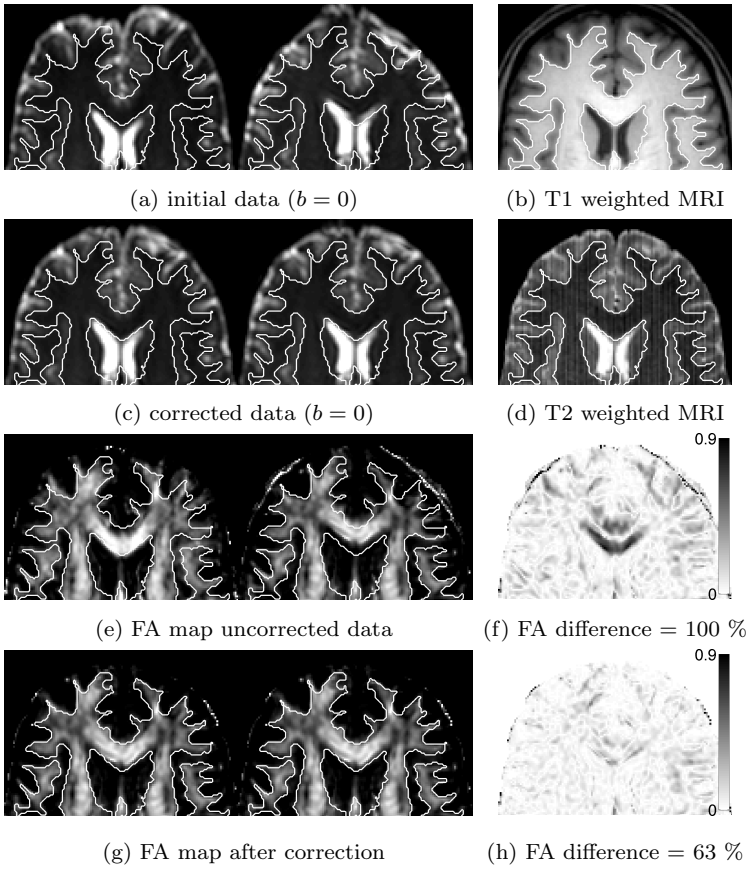

(a) initial data ($b = 0$) (b) T1 weighted MRI

(c) corrected data ($b = 0$) (d) T2 weighted MRI

(e) FA map uncorrected data (f) FA difference = 100 %

(g) FA map after correction (h) FA difference = 63 %

Figure 3. Registration result for dataset DTI-3 visualized in an axial slice, zoomed into the frontal brain region for better visibility. Contour lines representing a white matter segmentation are superimposed in all images excluding (f) and (h). Geometrical mismatch of the uncorrected $b = 0$ weighted diffusion weighted measurements (a) and T1w (b) and T2w (d) images is most severe in frontal regions and around the Corpus Callosum. After correction, geometrical correspondence improves crucially, see (c). Fractional anisotropy (FA) maps computed from both DTI measurements with reversed spatial encoding gradients without susceptibility correction and their absolute difference are shown in (e) and (f). As to be expected the FA maps are not well aligned to the white matter segmentation, especially around the Corpus Callosum. After correction, localization of the fractional anisotropy on the segmented white matter improves notably, see (g). This also manifests in a reduction of the absolute difference before (f) and after (h) correction (identical colormap).

3.3. Impact of the new regularization functional

We compared our method with the proposed nonlinear regularization term to the diffusion regularized scheme proposed in (Holland et al. 2010), obtained by setting $\beta = 0$ in (8). To this end, we varied the weight α on the diffusion regularizer $\mathcal{S}^{\text{diff}}$ between 1 and 70 and compared the image distance after correction $\mathcal{D}(B^\alpha)$ and the range of $\partial_{\mathbf{v}} B^\alpha$ for three scenarios for $\beta = 0, 1, 10$. In order to safe computation time for this parameter study, only two multi-level steps with discretizations of $m_1 = (32, 32, 36)$ and

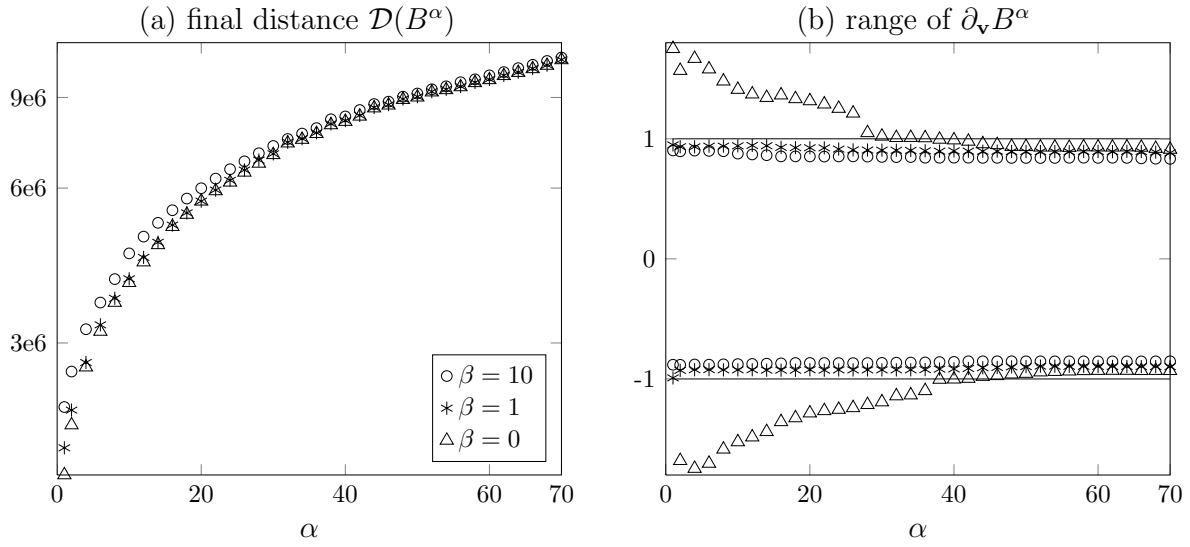

Figure 4. Comparison of diffusion regularization scheme ($\Delta\ \beta = 0$) as in Holland *et al* 2010 with the proposed extension by the nonlinear regularization term $\mathcal{S}^{\text{jac}}$ in (7) ($*\ \beta = 1 \circ \beta = 10$). The final image distances, depicted in a semi logarithmic plot (a) for α increasing from 1 to 70, is at a comparable level for all tested choices of β. As to be expected the image distance is reduced marginally more for $\beta = 0$. However, in plot (b), visualizing the range of $\partial_{\mathbf{v}} B^\alpha$, it can be seen that the regularity condition (6) is violated for $\beta = 0$ and small values of α. For $\beta = 1, 10$ the range is in the interval $[-0.99, 0.84]$ for all tested α.

$m_2 = (64, 64, 36)$ were performed.

Figure 4 (a) shows the final value of the distance functional (3) with increasing values for α on a semi logarithmic scale. The image distance is at a comparable level for all three choices of β with, as to be expected, marginally smaller values for $\beta = 0$. However, for $\beta = 0$ and too small values of α violations of the regularity criterion (6) occur. For $\beta = 1, 10$ the range of $\partial_{\mathbf{v}} B^\alpha$ was in the interval $[-0.99, 0.84]$. Thus the criterion (6) was fulfilled for all tested α after adding the novel nonlinear regularization functional.

4. Discussion

In the present work a diffeomorphic susceptibility correction algorithm for diffusion weighted MRI was developed, implemented and evaluated on a set of distorted data. The key novelty of the method is an additional nonlinear regularizer that guarantees positive intensity modulations and diffeomorphic geometrical transformations independent on the actual choice of regularization parameters. Incorporating the physical distortion model and reversed gradient method into a variational image registration framework yielded an efficient algorithm that computes smooth and meaningful estimates of the field-inhomogeneity. The correction approach effectively reduced the distortions in all

six brain DTI datasets obtained from widely applied clinical routine imaging protocol. We showed that a simple rigid registration is sufficient to register the corrected diffusion weighted data to T1- and T2-weighted images.

The extent of the spatial distortions is a result of the very small bandwidth of EPI sequences in phase-encoding direction. In a clinical setting, the drawback of severe distortions, typically in the frontal region, are accepted in exchange for the clinically required speed of EPI. Distortions are less pronounced in more central brain regions, and are often acceptable for diagnostics without in-depth quantitative evaluation. The extent of the distortions may be reduced by the use of techniques like parallel imaging (Prüssmann 2006) or segmented EPI acquisition (Atkinson et al. 2000), which is not always feasible, and significant distortions remain nevertheless.

In contrast to the approaches (Chang & Fitzpatrick 1992), (Morgan et al. 2004) and (Weiskopf et al. 2005), our proposed algorithm does not rely on pre-segmentation and edge-detection which is difficult especially in frontal regions, where in either $\mathcal{I}_1$ or $\mathcal{I}_2$ the signal is wrongly localized outside the head. Due to the intensity modulation, this stretching, however, is followed by a reduction of intensity, complicating the threshold-based segmentation. Compared to the 3D reversed gradient approaches in (Andersson et al. 2003) and (Skare & Andersson 2005), computational expenses were lowered due to both the non-parametric transformation model and the use of high-end optimization and multi-level techniques. As indicated by (Olesch et al. 2010, Holland et al. 2010) non-parametric transformation models are capable of estimating high gradients of the field inhomogeneity which was crucial for our distorted test data.

The proposed method can be understood as an extension of the recently presented variational approach (Holland et al. 2010) by a nonlinear regularization term that guarantees diffeomorphic geometrical transformations. In a numerical example we showed that this extension was crucial to obtain meaningful solutions for the distorted data, see Section 3.3. On the other side, our extension requires a second regularization parameter, which, at first glance, could be seen as a rather big disadvantage for broader practical application. However, as we showed, the new method turned out to be very stable with regard to the choice of the regularization parameters. With the presented fixed choice of both parameters, we obtained good results for all tested datasets. Future investigations will show, how much our new method is able to contribute to datasets from other diffusion weighted sequences, e.g., datasets constructed from raw data acquired with parallel imaging (Prüssmann 2006), and if our presented fixed choice of regularization parameters is also sufficient for such datasets and for datasets with different imaging parameters.

Although only the image pair without diffusion gradient is used for our correction, we acquired two full data sets with reversed phase- and frequency encoding gradients for each subject to investigate the impact of the correction on clinically relevant measures such as the fractional anisotropy. Hence, measurement time increased by 8 min for the full data set with 20 directions. Notably, the necessary additional data acquisition needed for distortion correction requires only about 1 min. If one relaxes the requirement

that the "flat" diffusion gradient be acquired with more signal averages than the steep gradients as proposed in (Jones 2004), the additional time requirement may be even shorter. Moreover, it does not increase with the number of gradient directions.

We like to mention that the correction technique is not limited to susceptibility correction in diffusion weighted MRI or even EPI, as the underlying physical distortion model was first developed for compensation of any inhomogeneity-induced localization errors in MR sequences (Chang & Fitzpatrick 1992).

Problems due to possible head movements between the acquisitions of $\mathcal{I}_1$ and $\mathcal{I}_2$ are neglected in our study as both images are consecutively acquired using fast EPI imaging within a sufficiently short time. If this assumption fails to hold, severe complications may arise from the fact that even small head rotations can lead to crucial image distortions in an inhomogeneous field (Jezzard & Clare 1999).

The transformation model (1) is mass-preserving, i.e., the total amount of intensity in both images is unaffected by the correction, see (Ruthotto 2010, Ch 2.1). Hence, it is assumed that no signal dropout occurs during the acquisition. This assumption is natural, since the distortion model only considers the mislocalization effect of the field inhomogeneity. Signal loss during the acquisition can thus be recovered neither by field map nor image-based correction approaches. While the assumption is well satisfied by spin echo data, see Section 2.6 , it is only approximately fulfilled by gradient echo schemes commonly used in functional MRI. Nevertheless, first preliminary numerical experiments suggest that our algorithm can also be used to improve the geometrical alignment and similarity for reversed gradient scans for fMRI data.

An important direction of future research will be the combination of our algorithm with methods correcting other important artifacts in DTI, e.g., due to eddy currents and vibration. In fact the acquisition schemes in (Bodammer et al. 2004, Mohammadi et al. 2011) are essentially equivalent to ours. Hence, no additional acquisition time is required.

5. Conclusion

We proposed a novel algorithm for susceptibility correction of diffusion weighted MRI based on a reversed gradient strategy. A novel nonlinear regularization functional guarantees diffeomorphic transformations and meaningful intensity modulations regardless of the actual choice of regularization parameters. In a DTI group study it is shown that the algorithm improves the image similarity between both reference scans and the geometric correspondence to anatomical images after a simple rigid registration. Our freely available implementation is highly efficient and correction of 3D volumes can be performed quickly on standard computers.

6. Acknowledgements

The authors would like to thank the anonymous reviewers for their helpful critics

and comments that significantly improved our manuscript. This research was partly supported by the German Research Foundation (DFG), projects WO1425/1-1,2-1,3-1, JU445/5-1 and BU 3227/2-1 and the collaborative research center (SFB) 656/B2. The authors would like to thank Fabian Gigengack for his help when starting the project.

Appendix: Existence of diffeomorphic solutions

In the following we prove that there exists at least one minimizer of the EPI functional and, most importantly, positive intensity modulations and diffeomorphic geometric transformations can be ensured due to the proposed nonlinear regularization functional. It is not obvious that the claimed strict inequalities in (6) hold for the limit. Consider, e.g., the sequence $\{\frac{1}{k}\}_{k\in\mathbb{N}}$, where each element in the sequence is strictly positive, however, the limit for $k \to \infty$ equals zero. Our proof uses the framework of direct methods in variational calculus. In order to keep the discussion focussed, we refer the interested reader to (Evans 1998, Ch. 8.2) for more details on the underlying theory.

Theorem 1. *Given images $\mathcal{I}_1, \mathcal{I}_2 \in \mathcal{C}^1(\Omega, \mathbb{R})$ and regularization parameters $\alpha, \beta > 0$. Assume that the objective functional $\mathcal{J}$ in (8) is finite for the zero displacement, i.e., $\mathcal{J}(\mathbf{0}) < \infty$.*

Then there exists at least one minimizer B^* of $\mathcal{J}$ in the set

$$\mathcal{A} = \left\{ B \in W^{1,2}(\Omega, \mathbb{R}) \mid \frac{1}{|\Omega|} \int |B(\mathbf{x})| d\mathbf{x} \leq K \text{ and } |\partial_{\mathbf{v}} B(\mathbf{x})| < 1 \text{ a.e. in } \Omega \right\}, \quad \text{(A.1)}$$

where the constant $K \in [0, \infty]$ bounds the mean magnitude of feasible inhomogeneities.

Proof. In order to show existence of minimizers in the Sobolev space $W^{1,2}(\Omega, \mathbb{R})$, we verify that the objective functional $\mathcal{J}$ is coercive, i.e., $\mathcal{J}$ grows sufficiently fast, and is lower semicontinuous, see (Evans 1998, Ch. 8.2).

Noting that all summands in $\mathcal{J}$ are positive, the diffusion regularizer $\mathcal{S}^{\text{diff}}$ is essential to obtain coercivity

$$\mathcal{J}(B) = \mathcal{D}(\mathcal{I}_1, \mathcal{I}_2; B) + \alpha \mathcal{S}^{\text{diff}}(B) + \beta \mathcal{S}^{\text{jac}}(B) \geq \alpha \mathcal{S}^{\text{diff}}(B) = \alpha \|\nabla B\|^2_{L^2}. \quad \text{(A.2)}$$

In order to derive a lower bound with respect to the $W^{1,2}(\Omega, \mathbb{R})$ norm we apply a generalized Poincaré inequality, (Evans 1998, p.275), denote the new constant by $C > 0$, and apply the triangle inequality

$$\begin{aligned}
\mathcal{J}(B) &\geq C(\|\nabla B\|^2_{L^2} + \left\| B - \frac{1}{|\Omega|} \int B(\mathbf{x}) d\mathbf{x} \right\|^2_{L^2}) && \text{(A.3)} \\
&\geq C(\|\nabla B\|^2_{L^2} + \|B\|^2_{L^2}) - C \left\| \frac{1}{|\Omega|} \int B(\mathbf{x}) d\mathbf{x} \right\|^2_{L^2} && \text{(A.4)} \\
&\geq C\|B\|^2_{W^{1,2}} - |\Omega| C \left(\frac{1}{|\Omega|} \int |B(\mathbf{x})| d\mathbf{x} \right)^2. && \text{(A.5)}
\end{aligned}$$

By using the boundedness of the mean absolute displacement (first condition in (A.1)) we finally see that $\mathcal{J}$ growth sufficiently fast with respect to the $W^{1,2}(\Omega, \mathbb{R})$ norm and is thus coercive

$$\mathcal{J}(B) \geq C\|B\|^2_{W^{1,2}} - |\Omega|C\left(\frac{1}{|\Omega|}\int |B(\mathbf{x})|d\mathbf{x}\right)^2 \geq C\|B\|^2_{W^{1,2}} - |\Omega|C\ K^2. \tag{A.6}$$

Lower semicontinuity of $\mathcal{J}$ follows directly from the convexity of the integrand with respect to ∇B. In combination, coercivity and lower semicontinuity yield the existence of a minimizer B^* in $W^{1,2}(\Omega, \mathbb{R})$ (Evans 1998, p. 448f).

The most important part, i.e., that B^* actually belongs to $\mathcal{A}$, remains to be shown. Bounding the mean magnitude of B^* is less critical. It follows directly from the convexity and continuity of the mapping $B \mapsto \frac{1}{|\Omega|}\int |B(\mathbf{x})|d\mathbf{x}$. The challenging part is to verify that B^* fulfills the regularity requirement (6). To this end, we fix a sufficiently small $\epsilon > 0$ and consider the set

$$S_\epsilon := \{\mathbf{x} \in \Omega \mid |\partial_{\mathbf{v}} B^*(\mathbf{x})| \geq 1 - \epsilon\}. \tag{A.7}$$

We finally bound the volume of S_ϵ by computing

$$\beta\ \phi(1-\epsilon)|S_\epsilon| = \beta \int_{S_\epsilon} \phi(1-\epsilon)d\mathbf{x} \leq \beta \int_{S_\epsilon} \phi(\partial_{\mathbf{v}} B^*(\mathbf{x}))d\mathbf{x} \leq \mathcal{J}(B^*) \leq \mathcal{J}(\mathbf{0}) < \infty. \tag{A.8}$$

Hence $|S_\epsilon| \leq \mathcal{J}(\mathbf{0})/(\beta\phi(1-\epsilon))$ and due to the growth behavior of $\phi(z) \to \infty$ as $|z| \to 1$ this yields that S_0 must be a set of volume zero and thus B^* fulfills (6) almost everywhere. □

References

Andersson J, Hutton C, Ashburner J, Turner R & Friston K 2001 *NeuroImage* **13**(5), 903–919.

Andersson J, Skare S & Ashburner J 2003 *NeuroImage* **20**(2), 870–888.

Atkinson D, Porter D, Hill D, Calamante F & Conelly A 2000 *Magnetic Resonance in Medicine* **44**(1), 101–109.

Basser P, Mattiello J & LeBihan D 1994 *Biophysical Journal* **66**(1), 259–267.

Bergui M, Zhong J, Bradac G & Sales S 2011 *Neuroradiology* **43**(10), 824–829.

Bodammer N, Kaufmann J, Kanowski M & Tempelmann C 2004 *Magnetic Resonance in Medicine* **51**(1), 188–193.

Chang H & Fitzpatrick J 1992 *IEEE Transactions on Medical Imaging* **11**(3), 319–329.

Conturo T, Lori N, Cull T, Akbudak E, Snyder A, Shimony J, McKinstry R, Burton H & Raichle M 1999 *Proceedings of the National Academy of Sciences of the United States of America* **96**(18), 10422.

De Munck J, Bhagwandien R, Muller S, Verster F & Van H 1996 *IEEE Transactions on Medical Imaging* **15**(5), 620–627.

Deppe M, Duning T, Mohammadi S, Schwindt W, Kugel H, Knecht S & Ringelstein E 2007 *Investigative radiology* **42**(6), 338.

Deppe M, Kellinghaus C, Duning T, Möddel G, Mohammadi S, Deppe K, Schiffbauer H, Kugel H, Keller S, Ringelstein E et al. 2008 *Neurology* **71**(24), 1981–1985.

Droske M & Rumpf M 2004 *SIAM Journal on Applied Mathematics* **64**(2), 668–687.

Duning T, Schiffbauer H, Warnecke T, Mohammadi S, Floel A, Kolpatzik K, Kugel H, Schneider A, Knecht S, Deppe M et al. 2011 *PloS one* **6**(3), e17770.

Edelstein W, Hutchison J, Johnson G & Redpath T 1980 *Physics in Medicine and Biology* **25**, 751.

Evans L 1998 *Partial Differential Equations* American Mathematical Society.

Gigengack F, Ruthotto L, Burger M, Jiang X, Wolters C H & Schäfers K P 2012 *IEEE Transactions on Medical Imaging* **31**(3), 698–712.

Güllmar D, Haueisen J & Reichenbach J 2010 *NeuroImage* **51**(1), 145–163.

Heidemann R, Porter D, Anwander A, Feiweier T, Heberlein K, Knösche T & Turner R 2010 *Magnetic Resonance in Medicine* **64**(1), 9–14.

Holdefer R, Sadleir R & Russell M 2006 *Clinical Neurophysiology* **117**(6), 1388–1397.

Holland D, Kuperman J & Dale A 2010 *NeuroImage* **50**(1), 175–183.

Hu X, Hu C, Fang X, Cui L & Zhang Q 2008 *Clinical Radiology* **63**(7), 813–818.

Hutton C, Bork A, Josephs O, Deichmann R, Ashburner J & Turner R 2002 *NeuroImage* **16**(1), 217–240.

Jezzard P & Balaban R 1995 *Magnetic Resonance in Medicine* **34**(1), 65–73.

Jezzard P & Clare S 1999 *Human Brain Mapping* **8**(2-3), 80–85.

Jones D 2004 *Magnetic Resonance in Medicine* **51**(4), 807–815.

Kaden E, Knösche T & Anwander A 2007 *NeuroImage* **37**(2), 474–488.

Kumar A, Welti D & Ernst R 1975 *Journal of Magnetic Resonance* **18**(1), 69–83.

Le Bihan D, Mangin J, Poupon C, Clark C, Pappata S, Molko N & Chabriat H 2001 *Journal of Magnetic Resonance Imaging* **13**(4), 534–546.

Liang Z & Lauterbur P 2000 *Principles of Magnetic Resonance Imaging: A Signal Processing Approach* IEEE Press New York.

Makuuchi M, Bahlmann J, Anwander A & Friederici A 2009 *Proceedings of the National Academy of Sciences* **106**(20), 8362–8367.

M.Burger, J.Modersitzki & L.Ruthotto 2012 *under revision, SIAM Journal of Scientific Computing* .

Merhof D, Soza G, Stadlbauer A, Greiner G & Nimsky C 2007 *Medical Image Analysis* **11**(6), 588–603.

Modersitzki J 2009 *FAIR: Flexible Algorithms for Image Registration* SIAM Philadelphia. Code freely available at: http://www.siam.org/books/fa06/.

Mohammadi S, Nagy Z, Hutton C, Josephs O & Weiskopf N 2011 *Magnetic Resonance in Medicine* . in press, DOI: 10.1002/mrm.23308.
URL: `http://dx.doi.org/10.1002/mrm.23308`

Morgan P, Bowtell R, McIntyre D & Worthington B 2004 *Journal of Magnetic Resonance Imaging* **19**(4), 499–507.

Mori S, Kaufmann W, Pearlson G, Crain B, Stieltjes B, Solaiyappan M & Van Zijl P 2000 *Annals of Neurology* **47**(3), 412–414.

Neumann-Haefelin T, Wittsack H, Wenserski F, Siebler M, Seitz R, Mödder U & Freund H 1999 *Stroke* **30**(8), 1591–1597.

Nocedal J & Wright S 2000 *Numerical optimization* Springer.

Olesch J, Ruthotto L, Kugel H, Skare S, Fischer B & Wolters C 2010 *in* 'Proc. SPIE 7623, 76230K, DOI:10.1117/12.844375'.

Opitz A, Windhoff M, Heidemann R, Turner R & Thielscher A 2011 *NeuroImage* **58**(3), 849–859.

Prüssmann K 2006 *NMR in Biomedicine* **19**(3), 288–299.

Qing-San Xiang F 2007 *Magnetic Resonance in Medicine* **57**(4), 731–741.

Robson M, Gore J & Constable R 1997 *Magnetic Resonance in Medicine* **38**(5), 733–740.

Ruthotto L 2010 Mass-preserving registration of medical images German diploma thesis (mathematics, written in english) Institute for Computational and Applied Mathematics, University of Münster. http://wwwmath.uni-muenster.de/num/publications/2010/Rut10/.

Shimony J S, McKinstry R, E.Akbudak, J.A.Aronovitz, A.Z.Snyder, N.F.Lori, T.S.Cull & T.E.Conturo 1999 *Radiology* **212**(3), 770–784.

Skare S & Andersson J 2005 *Magnetic Resonance in Medicine* **54**(1), 169–181.

Skare S, Hedehus M, Moseley M & Li T 2000 *Journal of Magnetic Resonance* **147**(2), 340–352.

Smith S, M.Jenkinson, Woolrich M, Beckmann C, Behrens T, Johansen-Berg H, Bannister P, De Luca M, Drobnjak I, Flitney D, Niazy R, Saunders J, Vickers J, Zhang Y, De Stefano N, Brady J & Matthews P 2004 *NeuroImage* **23**, S208–S219.
URL: `http://www.sciencedirect.com/`

Stehling M, Turner R & Mansfield P 1991 *Science* **254**(5028), 43.

Stejskal E & Tanner J 1965 *The Journal of Chemical Physics* **42**(1), 288–292.

Tao R, Fletcher P, Gerber S & Whitaker R 2009 *in* 'Information Processing in Medical Imaging' Springer pp. 664–675.

Warach S, Chien D, Li W, Ronthal M & Edelman R 1992 *Neurology* **42**(9), 1717.

Weiskopf N, Klose U, Birbaumer N & Mathiak K 2005 *NeuroImage* **24**(4), 1068–1079.

Wersching H, Duning T, Lohmann H, Mohammadi S, Stehling C, Fobker M, Conty M, Minnerup J, Ringelstein E, Berger K et al. 2010 *Neurology* **74**(13), 1022–1029.

Wiegell M, Tuch D, Larsson H & Wedeen V 2003 *NeuroImage* **19**(2), 391–401.

Wieshmann U, C.A.Clark, M.R.Symms, F.Franconi, G.J.Barker & S.D.Shorvon 1999 *Magnetic Resonance Imaging* **17**(9), 1269–1274.

Wolters C, Anwander A, Weinstein D, Koch M, Tricoche X & MacLeod R 2006 *NeuroImage* **30**(3), 813–826.

Zaitsev M, Hennig J & Speck O 2004 *Magnetic Resonance in Medicine* **52**(5), 1156–1166.

Zeng H & Constable R 2002 *Magnetic Resonance in Medicine* **48**(1), 137–146.